The application of distributed optical fiber sensors (BOTDA) to sinkhole monitoring. Review and the case of a damaging sinkhole in the Ebro Valley evaporite karst (NE Spain)

Francisco Gutiérrez (1)*, Jorge Sevil (1), Pascual Sevillano (2), Javier Preciado-Garbayo (3,4), Juan J. Martínez (4), Sonia Martín-López (5), Miguel González-Herráez (5)

(1) Department of Earth Sciences; University of Zaragoza; 50009 Zaragoza; Spain

(2) Aragon Institute of Engineering Research (I3A), University of Zaragoza; 50018 Zaragoza; Spain

(3) Electronic Engineering and Communications Department, EINA, University of Zaragoza; 50018 Zaragoza; Spain

(4) Aragon Photonics Labs., 50009 Zaragoza, Spain,

(5) Department of Electronics, Escuela Politécnica Superior, Universidad de Alcalá, 28805 Madrid, Spain

* Corresponding author e-mail: fgutier@unizar.es

Abstract

Distributed optical fiber sensors (DOFS) have been postulated as a suitable technique for long-range monitoring of sinkhole-related subsidence, and possibly for the anticipation of catastrophic collapse (early-warning systems). The strain data published in previous works refer to artificial experiments considering real and virtual cover collapse sinkholes characterized by rapid subsidence and sharp lateral deformation gradients. The influence of the subsidence mechanism (sagging, collapse, suffosion) on the capability of DOFS to satisfactorily detect active subsidence is discussed. Sagging sinkholes with poorly-defined lateral edges, low lateral deformation gradients and slow subsidence are identified as the most challenging scenario. The performance of BOTDA optical fiber for monitoring such type of sagging sinkholes is evaluated in the active Alcalá sinkhole, which affects a flood-control dike creating a high-risk and -uncertainty scenario. This sinkhole shows active subsidence in sections tens of meters long with maximum subsidence rates ranging between 5 and 35 mm/yr. The comparison of vertical displacement data measured by high-precision leveling and the strain recorded by two types of fiber optic cables shows good spatial and temporal correlation. The subsidence sections are

captured in the strain profiles by: (1) troughs of negative strain (contraction) in the area affected by subsidence, with the maximum strain associated with the point of most rapid settlement; and (2) lateral ridges of positive values (extension) in the marginal zones. A subsidence acceleration phase associated with a flood is also captured by substantial increments in the strain values. In this challenging scenario, despite the reasonably good spatial and temporal correlation between the displacement and strain data, the unambiguous identification of the active subsidence area with the fiber optic data alone might be difficult. Better results could be obtained improving the monitoring system (e.g., tighter cable-ground coupling) and testing other types of sinkholes with more localized deformation zones and higher subsidence rates.

Key words: fiber optic sensing, collapse anticipation, sinkhole hazard, sinkhole remediation, evaporite karst

1. Introduction

Ground deformation monitoring is an important task for various aspects related to sinkhole risk management, including preventive planning, selection of remediation measures and assessment of their performance, design of subsidence-proof structures, or implementation of early-warning systems. Monitoring systems may face two main types of scenarios: (1) Measurements are collected at known sinkholes or sinkhole sites. Ideally, the gathered data should allow the delineation of the areas affected by settlement, the measurement of subsidence rates and their spatial-temporal variability with sufficient accuracy and resolution. (2) A more challenging scenario is that in which monitoring systems seek to detect and locate new sinkholes in their initial stages. Often, these schemes are aimed at capturing precursory ground deformation preceding sudden collapse, serving as an early-warning system (e.g., Malovichko et al., 2009; Jones and Blom, 2014; Baer et al., 2018). The anticipation of catastrophic collapse occurrence together with timely evacuations or service interruptions may help to prevent fatalities. Recently, the potential societal risks associated with the construction of transport infrastructure (e.g., vulnerable high-speed railways) in vast sinkhole-prone areas are receiving special attention (Guan et al., 2015; Jiang et al., 2016). A key practical question is whether it would be possible to detect sinkhole-related deformation sufficiently in advance to prevent accidents. Important issues that should be considered in the design of sinkhole monitoring systems are the subsidence mechanisms and the associated deformation style and kinematics. For instance, collapse that produces deformation with sharp lateral gradients makes its detection easier. In

contrast, sagging sinkholes are characterized by vaguely-edged subsidence areas with subtle horizontal variations in deformation that may be uneasy to pinpoint. Regarding the kinematics, sinkholes may experience: (1) one-time catastrophic collapse; (2) step-wise incremental displacements; (3) gradual settlement; or (4) a combination of the former. Interestingly, some of the highest subsidence rates have been measured in sagging sinkholes related to salt dissolution (Al-Halbouni et al., 2017; Desir et al., 2018; Gutiérrez et al., 2019).

The most widely used monitoring methods suffer from a number of limitations to satisfactorily function as early-warning systems (see review in Gutiérrez et al., 2019): (1) spatial and temporal resolution may be insufficient to capture short-duration precursory deformation and spatially restricted sinkholes (e.g., DInSAR; Theron et al., 2017); (2) areal or longitudinal extent covered by the measurements may be insufficient to monitor large sites or long linear infrastructure (e.g., high-precision leveling, terrestrial laser scanner; Sevil et al., 2021); and (3) inability to provide automatically-gathered real-time data (e.g., Structure from Motion Photogrammetry; Schwendel and Cooper, 2021). Potentially, these limitations might be overcome by using distributed optical fiber sensors, which is a promising approach still in an experimental and evaluation phase for sinkhole monitoring.

Distributed optical fiber sensors (DOFS) have been satisfactorily used to detect and monitor various types of ground instability phenomena such as landslides (Zhao et al., 2021), seepage-related piping (Inaudi, 2014), or subsidence induced by tunneling (Asaf et al., 2014, Xin et al., 2021) or mining (Naruse et al., 2007). These methods have also been tested for sinkhole monitoring via physical laboratory models and numerical simulations, but to our knowledge no case studies showing the practicality of the technique in active sinkholes under natural conditions have been published (see review below). In the DOFS based on the Brillouin Scattering, a coherent light pulse emitted by a laser at one extreme of the sensor travels through the fiber generating the Brillouin effect along its entire length. The Brillouin effect is related to the excitation of acoustic modes in the crystalline structure of the optical fiber. This inelastic scattering produces short lasting acoustic waves and backscattered light, the frequency of which is downshifted from the impinging light (Yeniay et al., 2002). The frequency difference between the emitted and the backscattered light is called the Brillouin frequency shift (BFS, $\Delta\nu_B$), which is related to the local temperature and strain in the fiber

$$\Delta\nu_B = C\varepsilon\Delta\varepsilon + C_T\Delta_T$$

where $C\varepsilon$, C_T are the strain and temperature sensitivity coefficients, and $\Delta\varepsilon$, Δ_T are the local strain and temperature increment loaded on the optical fiber (Culverhouse et al., 1989; Horiguchi et

al., 1989). In the Brillouin Optical Time Domain Analysis (BOTDA) scheme a counter-propagating light is introduced at the other end of the fiber to stimulate the scattering process and increase the intensity of the backscattered light. This allows the accuracy in the measurement of the frequency shift to be improved (Hartog, 2017). A distributed measurement of the Brillouin frequency shift along the optical fiber can be resolved from the time elapsed between the launch of the light pulse and the arrival of the backscattered light. As indicated above, the Brillouin frequency shift integrates both temperature and strain effects. The temperature contribution in the BFS shift between campaigns can be compensated by installing temperature sensors or optic fiber cables that are not affected by strain (e.g., loose-tube cables) (Zhou et al., 2008). When considering the application of optical fiber systems to sinkhole monitoring, a good mechanical coupling between the sensor and the surrounding material should be achieved, so that the strain in the fiber reliably records the ground deformation or the structural damage. Strain-sensing fibers can also be embedded in tapes or geotextiles to improve the adherence with the surrounding medium (Inaudi, 2014). A non-straightforward issue is to transform the axial strain measured in the fiber into the deformation related to sinkhole activity, dominated by downward vertical displacement (subsidence). This can be performed by developing strain-displacement models as illustrated by Chen et al. (2020) in laboratory experimental models.

The first part of this work reviews previous experiences related to the application of distributed optical fiber sensors to sinkhole monitoring, stressing the critical role that subsidence mechanism (i.e., sinkhole type) and rates may play on the performance of the technique. The second part illustrates the application of Brillouin Optical Time Domain Analysis (BOTDA) to an active slow-moving sagging sinkhole, and evaluates its performance comparing the strain recorded by fiber cables with the subsidence measured by high-precision leveling.

2. Subsidence mechanisms and their potential signature on fiber sensors

To our knowledge, all the published works dealing with the application of optical fiber sensors to sinkhole monitoring are based on artificial physical models or numerical models of cover collapse sinkholes, disregarding other types of sinkholes. However, sinkholes may form by various subsidence mechanisms that determine the spatial and temporal patterns of the strain affecting the fiber. Subsidence sinkholes related to subsurface mass depletion by dissolution can be classified indicating two descriptors (Gutiérrez, 2016; De Waele and Gutiérrez, 2022). The first one refers to the type of material affected by downward displacement, including cover (unconsolidated surficial deposits), bedrock (karst rocks), and caprock (non-karst rocks). The

second term denotes the main subsidence mechanism, including collapse, sagging and suffosion. DOFS are particularly well suited for covered karst settings, where the soluble bedrock is mantled by a cover of unconsolidated deposits in which the sensing optical fibers can be easily deployed by excavating trenches (e.g., Shefchik et al., 2011). Cover deposits, either natural or anthropogenic, can be affected by any of the three subsidence mechanisms (**Fig. 1**).

Cover collapse sinkholes may display two end-member deformation styles relevant to optical-fiber monitoring (**Fig. 1**). The most common mechanism is the upward propagation of voids through a cohesive cover by successive cavity-roof collapse (i.e., stoping). In this situation, at an early stage, the soil in which the fiber is embedded can be undermined by an underlying cavity, experiencing a subtle deformation (e.g., cracking, bending, dilation). Eventually, the soil surrounding the sensor may breakdown and the fiber becomes suspended and decompressed, before the collapse reaches the surface (**Fig. 1**). In this scenario, increasing the depth or depth range of the fiber sensors would allow to prolong the anticipation time between the detection of the subsurface deformation and the occurrence of a collapse at the surface, improving the success rate of early warning systems. Another less common cover collapse deformation style is the foundering of integral blocks with limited internal deformation bounded by well-defined dip-slip failure planes typically with annular geometry (**Figs. 1, 2A, D**). In these sinkholes, subsidence affects the cover up to the ground surface, and strain in the fiber is expected to be particularly intense at the margins of the foundering block (i.e. shear zone), showing sharp lateral deformation gradients.

Sagging involves the progressive downward bending of ductile material situated above a dissolution zone (**Figs. 1, 2C**). This subsidence mechanism mostly occurs in evaporite karst areas, where subsurface dissolution of gypsum and/or salt may operate across relatively large areas. Cavities do not necessarily form beneath these sinkholes, since subsurface dissolution may be accompanied simultaneously by the sagging of the overlying material. In cover sagging sinkholes subsidence typically affects all the sedimentary pile above the dissolution zone up to the ground surface. Ground deformation typically shows poorly defined edges and limited lateral strain gradients. Passive bending associated with the sagging mechanism involves a centripetal contraction producing compression in the inner zone (i.e., maximum subsidence area), which is counterbalanced by radial extension at the margin (e.g., Gutiérrez et al., 2012, 2018; De Waele and Gutiérrez, 2022). Thus, the optical fiber is expected to suffer contraction and stretching in the central and marginal areas, respectively.

The development of cover suffosion sinkholes involves the downward migration of weak cover deposits through voids at the rockhead and the progressive settlement of the overlying material, either by plastic deformation or cohesionless granular flow (hourglass model) (**Figs. 1, 2B**). This spatially continuous deformation process may attenuate upwards, but is expected to propagate up to the ground surface soon after its initiation. Ground deformation in suffosion sinkholes tends to be spatially restricted (i.e., a few meters) and with significant lateral gradients. In many sinkholes found in nature, different subsidence mechanism may operate showing a wide range of spatial and temporal variations. For instance, a sinkhole may be affected simultaneously by sagging and collapse, or a slow sagging sinkhole may evolve into a catastrophic collapse sinkhole (**Fig. 2E**).

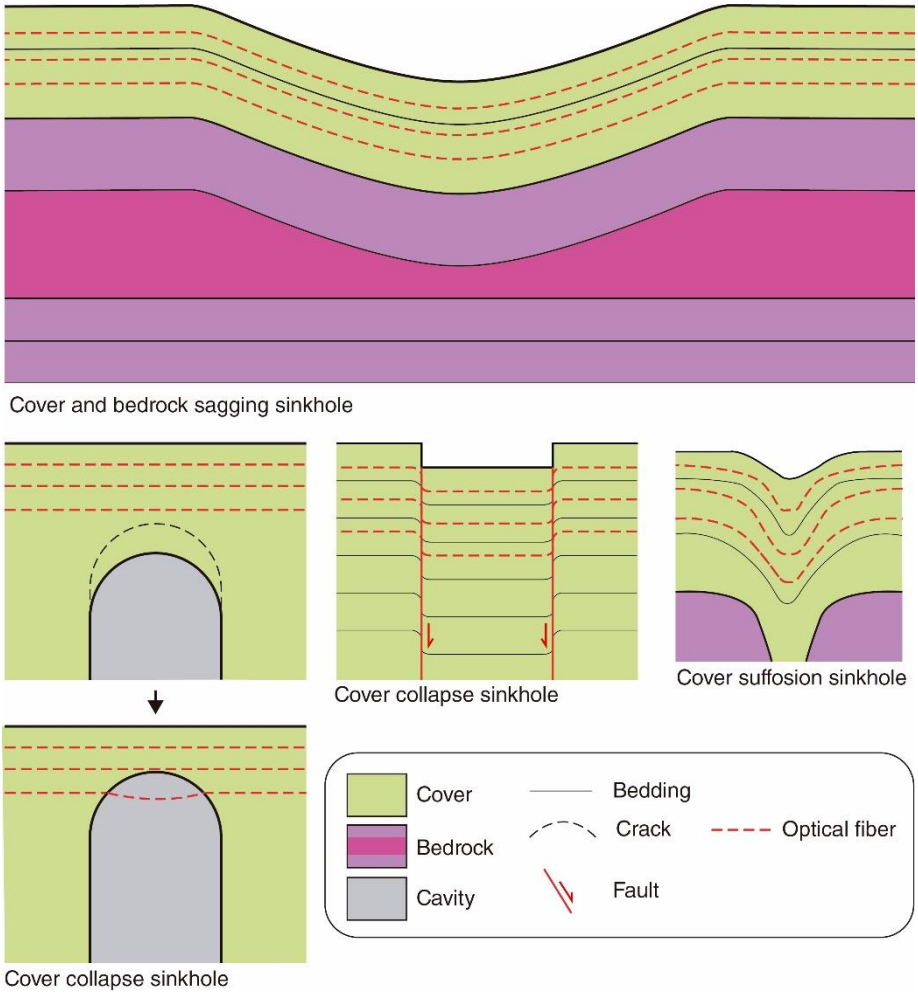

Figure 1. Diagrams showing the three main subsidence mechanisms that can be involved in the development of sinkholes in a covered karst setting (sagging, collapse, suffosion), and the expected deformation in optical fibers embedded at different depths in the cover. Note that cover collapse sinkholes may be related to the upward propagation of cavities by progressive cavity roof collapse (stoping), and the foundering of integral blocks with limited internal

178 deformation that extend up to the surface. Multiple combinations of these end-members can
179 be found in nature.

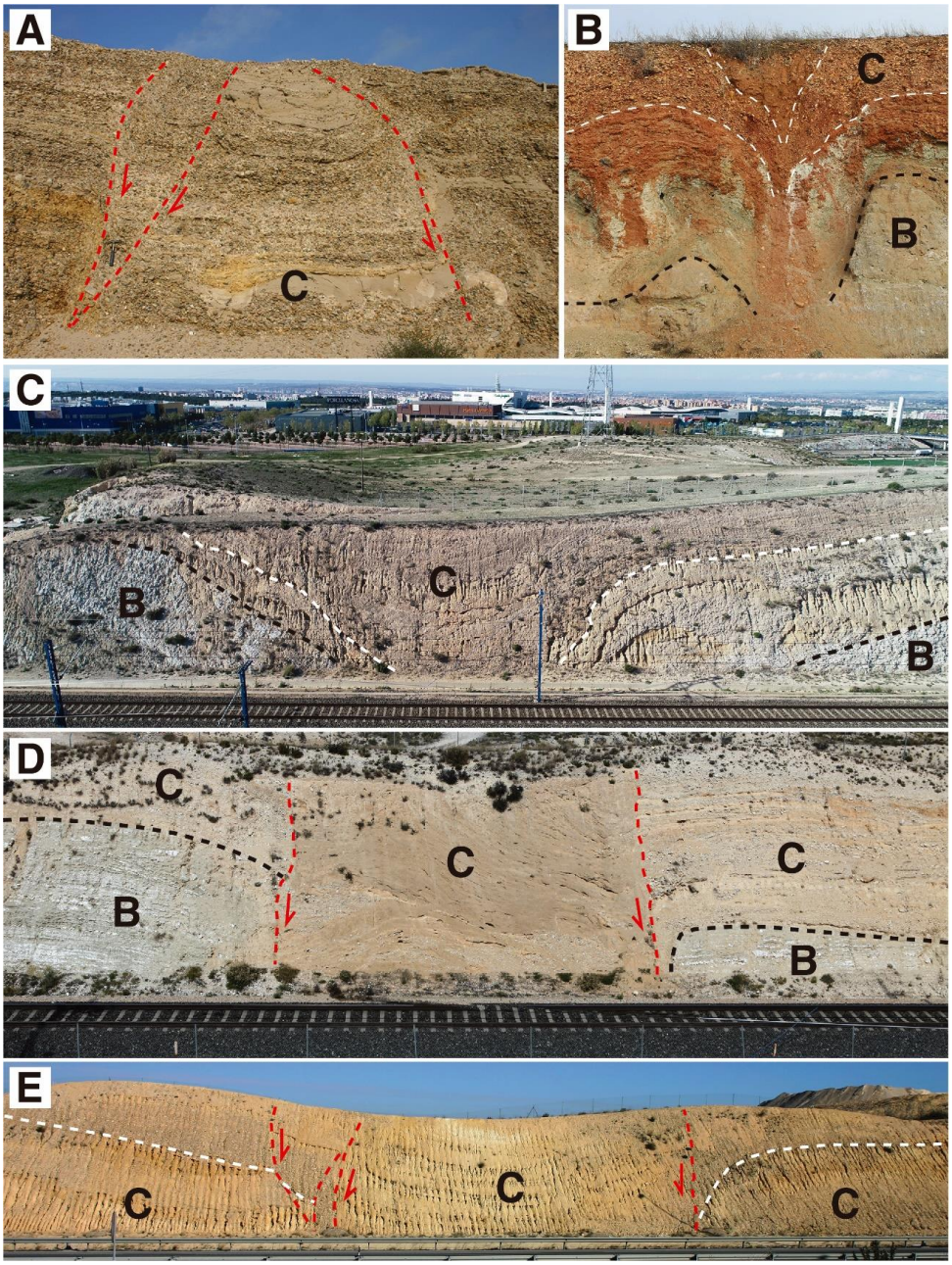

180

181 Figure 2. Artificial exposures of paleosinkholes from Spain illustrating various types of
182 subsidence mechanisms. Dashed black, white and red lines indicate the bedrock-cover contact,
183 bedding, and collapse faults, respectively. B and C stand for bedrock and cover. (A) Collapsed
184 block in gravel deposits bounded by outward dipping failure planes. (B) Cover suffosion
185 paleosinkhole related to the downward migration of weak cover deposits into solutional
186 conduits in gypsum bedrock. (C) Large sagging paleosinkhole exposed in the cuttings of the
187 Madrid-Barcelona high-speed railway at Zaragoza city. (D) Cover and bedrock collapse
188 paleosinkhole at the Madrid-Barcelona high-speed railway at Zaragoza city. (E) Cover sagging

189 and collapse paleosinkhole, showing that subsidence can be accommodated simultaneously or
190 sequentially by passive bending and the development of collapse faults.

191

192 **3. Previous experiences**

193 To the best of our knowledge, there are no accounts in the international literature of optical
194 fiber measurements of ground deformation in natural active sinkholes using DOFS. Shefchik et
195 al. (2011) reported on an early-warning system based on a 4 km long optical fiber deployed in
196 an area of Hutchinson city, Kansas. Here, several collapse sinkholes have formed above caverns
197 created by salt solution mining, threatening a major railway. Guan et al. (2015) described a 90
198 m long BOTDR sinkhole monitoring system installed in the Guilin-Yangshuo highway, built upon
199 cavernous limestone mantled by clayey soil. Jiang et al. (2016) reported that the Chinese
200 Institute of Karst Geology established in 2006 and 2012 two pilot monitoring sites at Guilin and
201 Guigang of Guangxi province to monitor potential sinkholes along a highway and an oil pipe,
202 respectively. However, no results have been published about these sites. The performance of
203 distributed optical fibers for sinkhole monitoring has only been assessed in three main types of
204 artificial experiments: (1) physical laboratory models that reproduce cover collapse sinkholes;
205 (2) physical models in which the sinkhole-related deformation is simulated by applying vertical
206 loads; and (3) numerical models that predict sequentially the ground deformation above a cavity
207 (i.e., deformation profile) and the expected signal that would be recorded by an optical fiber
208 sensor.

209 The experiments that reproduce cover collapse sinkholes in the laboratory use meter-sized
210 containers filled with soil, in which cavities are created beneath strain and temperature sensing
211 fibers (Lanticq et al., 2009; Jiang et al., 2016; Xu et al., 2017; Chen et al., 2020). Deformation in
212 the soil above the cavities is induced by applying a static load, adding percolating water, or
213 pumping water. In these tests the cover collapse sinkholes develop by the upward propagation
214 of cavities, resulting in the formation of small scarp-edged depressions up to 1.5 m across. The
215 strain recorded by the distributed optical fiber sensor is compared with vertical displacement
216 measurements to assess the performance of the approach. The results obtained in these
217 experiments show a good spatial and temporal correlation between the measured strain and
218 ground deformation, with the greatest values of the former in the central sector of the
219 subsidence area. Lanticq et al. (2009) tested Brillouin optical time-domain reflectometry
220 (BOTDR) and optical frequency-domain reflectometry (OFDR) above cavities 2 m across,
221 embedding the fibers in soil at different depths and with variable lateral offsets. The strain

measured in the fiber showed tensile areas flanking a compressive region above the cavities. They found that subsidence was detected earlier and with higher spatial accuracy with OFDR because of its greater spatial resolution. Moreover, they illustrated that meshes of cables are necessary to resolve the size and depth of cavities. Jiang et al. (2016), using optical fibers installed at different depths above the cavities, observed lower strain in the shallower sensors, attributable to the upward propagation of the deformation and the less effective cable-soil coupling in the upper cables, subject to lower load. Xu et al. (2017) observed sudden increases in the strain values attributable temporal variations in subsidence rate. Chen et al. (2020) developed a strain-displacement model, obtaining discrepancies between the displacement measured at the surface and that modeled with the strain sensed by the fiber below 14%.

In the second type of experiment, the sinkhole-related deformation is simulated by applying increasing loads at points with variable spacing to reproduce the axial strain in the fiber induced by cavities of variable span. Zhende et al. (2013) implemented this approach using conventional optical fiber and glassfiber reinforced plastic optical fiber to compare the performance of the two different types of sensors. They found that the conventional fiber allowed the area affected by sinkhole-related deformation to be more precisely delineated. The larger deformation zone detected by the reinforced fiber is attributed to lower friction and mechanical coupling between the sensor and the embedding soil. In the third type of experiment, Linker and Klar (2017) predicted deformation profiles in soils above cavities with a hemispherical roof using numerical mechanical models. On the basis of the ground displacement profiles, they modeled the expected strain signals that would be recorded by optical fiber sensors. These authors suggest that the performance of the technique for sinkhole detection could be improved by enhancing the components attributable to dissolution-induced subsidence using a library of synthetic reference signals, facilitating the discrimination of the undesired signals related to other disturbances.

4. The high-risk Alcalá sinkhole

The Alcalá village is located in the floodplain of the Ebro River in NE Spain, adjoining the outer side of a meander (**Fig. 3**). The analysis of aerial photographs from different dates reveals that the river channel experienced a shift of 540 m between 1927 and 1957, moving next to the village (Gutiérrez et al., 2019). From the geological perspective, the sinkhole site is situated in the central sector of the Ebro Cenozoic Basin. Here, the bedrock corresponds to the evaporitic Oligo-Miocene Zaragoza Formation. In the subsurface, it consists of anhydrite, halite, glauberite,

mudstone and marls. In outcrops, halite does not occur due to dissolution, and the evaporites are restricted to secondary gypsum derived from the hydration of anhydrite and the incongruent dissolution of glauberite (Salvany et al., 2007; Salvany, 2009). On the northern margin of the valley, where halite has been extensively mined since historical times (Remolinos village area), there is an evaporite unit around 28 m thick consisting of a glauberite-rich package around 19 m thick, overlain by a halite seam 9 m thick (Gutiérrez et al., 2022). The projection of this salt-rich unit from 3 km towards Alcalá, considering the apparent valleyward dip of the strata (0.53°; Gutiérrez et al., 2015), indicates that its top lies at a depth of approximately 20 m below the village. The presence of halite and glauberite in the bedrock beneath Alcalá village was documented by boreholes drilled for a geotechnical report by Quiles (2007). It should be noted that salt dissolution plays a critical role in the development of sinkholes and their subsidence activity, since the equilibrium solubilities of halite (NaCl) and glauberite ($CaNa_2(SO_4)_2$) are 356 g/L and 118 g/L, respectively, whereas that of gypsum ($CaSO_4 \cdot 2H_2O$) is 2.6 g/L (De Waele and Gutiérrez, 2022). The numerous boreholes drilled in the sinkhole site, with depths ranging between 25 m and 44 m, indicate the following lithological succession, in descending order (Gutiérrez et al., 2019): (1) 6-7 m of detrital cover made up of man-made fill and alluvium; (2) 20 m of dark clay and marls with residual gypsum particles, corresponding to a karstic residue; and (3) glauberite- and halite-bearing bedrock. A number of boreholes drilled in the streets next to the dike have penetrated meter-sized cavities, mostly concentrated at depths between 13 and 19 m.

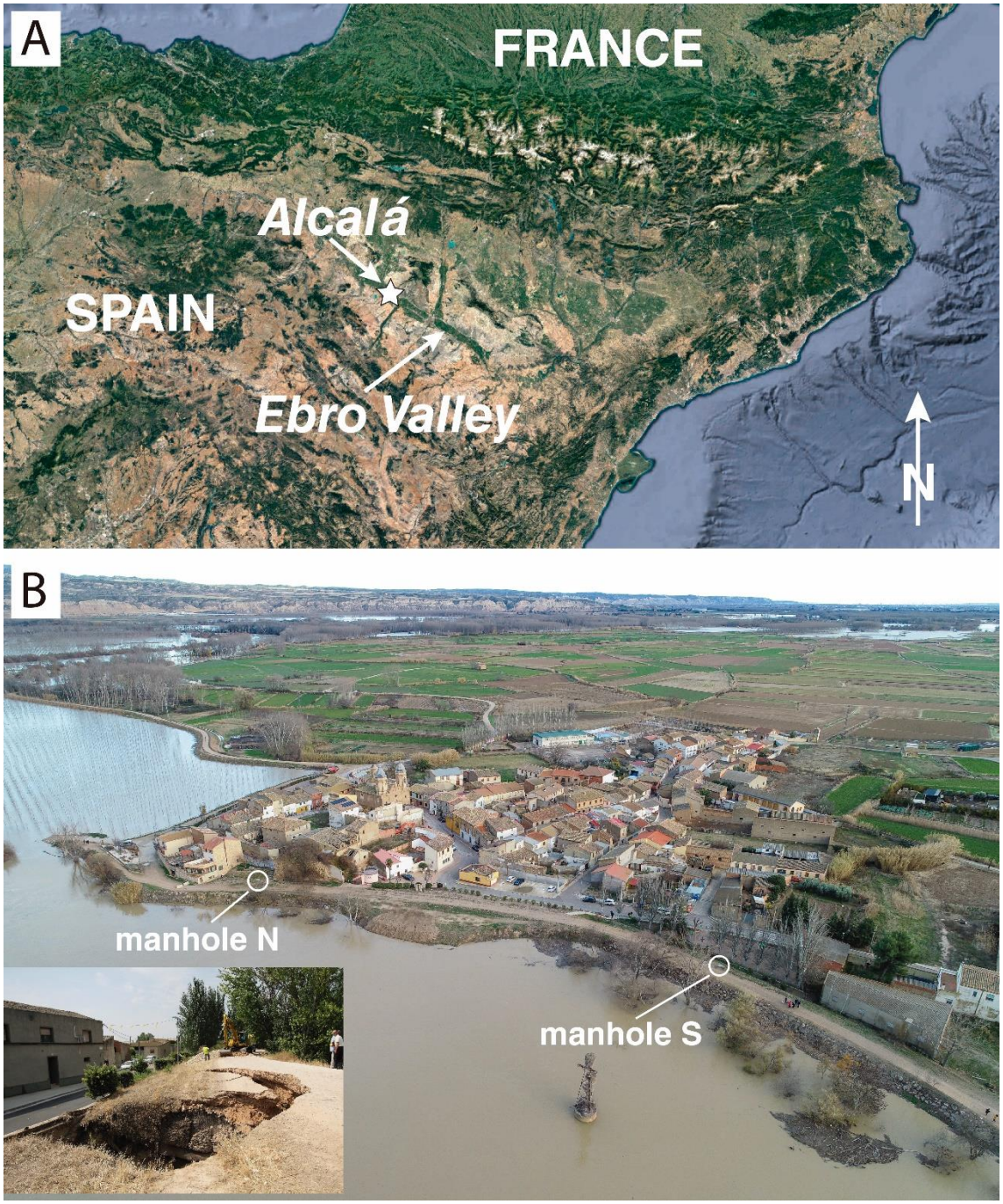

Figure 3. Setting of the Alcalá village and sinkhole. A: Location of Alcalá village in the Ebro Valley, within the central sector of the Ebro Cenozoic Basin (NE Spain) (Image downloaded from Google Earth). B: Oblique aerial view of Alcalá village on the outer side of a meander and protected by a flood-control dike. The sinkhole, situated between the two manholes, affects the dike and an adjacent portion of the village. Image taken during the December 2021 Ebro River flood. Inset shows the collapse sinkhole that occurred in the dike in November 2013.

The active Alcalá sinkhole is a sagging sinkhole (Gutiérrez, 2016) with vaguely-defined edges that affects a section more than 100 m long of the dike and an adjacent area in the village (**Fig. 3**).

Since 2007 the subsidence area has experienced multiple nested catastrophic collapses eventually leading to the demolition of a house, and it has been subject to several localized remediation measures (Benito-Calvo et al., 2018; Desir et al., 2018; Gutiérrez et al., 2019). In November 2013, the occurrence of a collapse sinkhole 9 m long and 4 m deep in the dike triggered the awareness of the high-risk and uncertainty situation created by the sinkhole, which could result in the failure of the dike during a flood (**Fig. 3B**). A review of the evolution of the sinkhole between 2007 and 2018 was presented by Gutiérrez et al. (2019), addressing: (1) the collapse events; (2) the damage caused by subsidence; (3) the remediation measures; and (4) the spatial-temporal variations of the subsidence monitored by high-precision leveling and terrestrial laser scanner, together with their relationships with the engineering measures and flood events. Two types of remediation measures have been applied in the sinkhole site: (1) shallow injection of high-expansion polyurethane foam above the cavities concentrated at 13-19 m depth, carried out in the streets (November-December 2013) and in the dike (November-December 2015); and (2) compaction grouting with high-viscosity mixtures reaching the depth of the cavities, complemented with high-tensile resistance geogrids, applied in the streets (December 2016-February 2017), and in a 50 m long section of the dike (December 2018-January 2019). Monitoring data collected since October 2014 indicates the following general patterns (Benito-Calvo et al., 2018; Gutiérrez et al., 2019): (1) substantial reduction of the subsidence after the application of deep compaction grouting, with subsidence rates dropping from tens of centimeters per year to centimeters per year; (2) acceleration and expansion of the subsidence in the dike induced by the injection of polyurethane foam above the cavities, aggravating the situation; and (3) phases of more rapid subsidence associated with flood events, especially during their recession and the accompanying water-table drop and buoyancy loss.

5. Monitoring deployment and methodology

The fiber optic cables were installed in four parallel trenches excavated along a 136 m long section of the dike crest (**Fig. 4**). The 0.4 m wide and 0.6 m deep backhoe trenches have a lateral separation of around 1.2 m and their trace at both extremes bend eastward and merge into a single trench connected to manhole N and manhole S in the north and south, respectively. From west (river side) to east (village side) the trenches are designated as A, B, C, and D. Two cables were deployed in each trench at different depths. The bottom cables were embedded within a 20 cm thick fill of well-graded sand. The upper cables were placed within a gravelly fill derived from the excavation of the trenches. Two similar types of tight-buffered armored cables were

used (**Figs. 4, 5**): (1) BRU cable with fiberglass armor (commercially named CDAD by the vendor, OPTRAL) in the bottom of trenches A, B, C; and (2) CSB cable with corrugated steel armor (commercially named CDAS by the vender, OPTRAL) in the bottom of trenches C and D and the upper level of all the trenches. Note that the bottom of trench C has both BRU and CSB connected with a splice due to insufficient supply of the former cable by the manufacturer. This mixed fiber cable section does not provide reliable data. The upper-level CSB cables in trenches A and D were placed within a pipe to prevent strain effects and isolate the temperature signal, thus the variation of the latter parameter can be compensated. The layout of the fiber optic cables with respect to the trenches and manholes is shown in **figure 5**. Both types of cables have a similar internal structure differentiated solely by the outer jacket of the cable. Having the same elements in the inner structure they both present similar mechanical and thermal sensitivity. The cables were chosen for their tight-buffered structure, which enhances a strong connection between the inner fibers and the rest of the cable. As a result, the fibers undergo deformation proportional to that experienced by the cable.

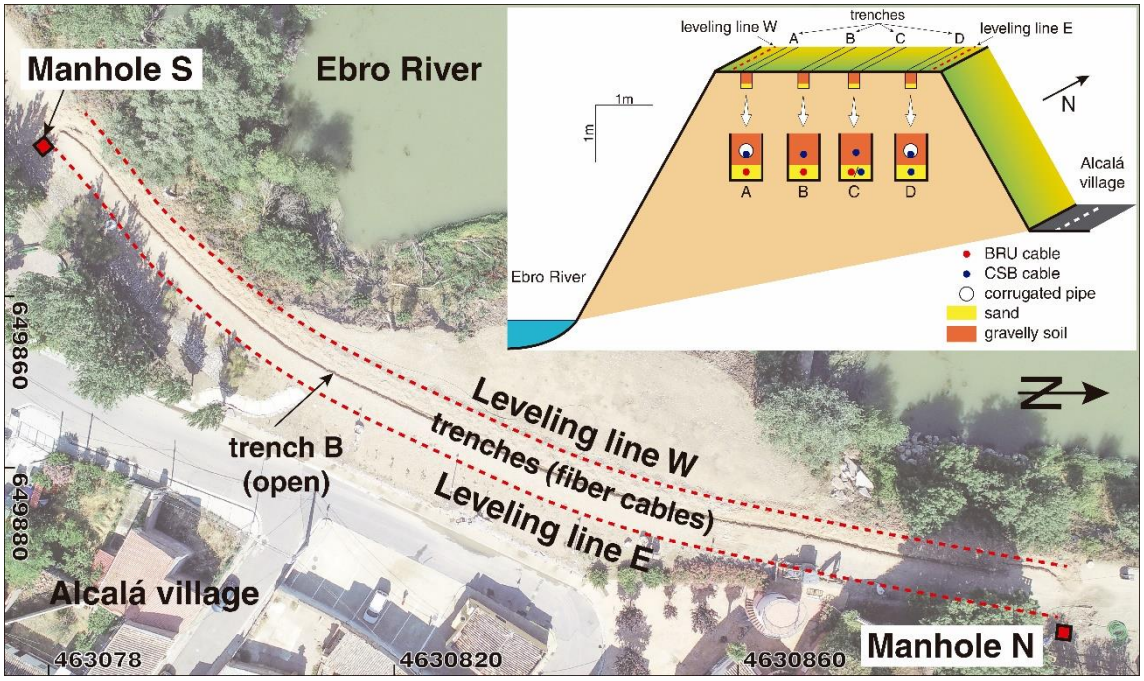

Figure 4. Orthoimage of the flood-control dike at Alcalá village showing the distribution of the leveling lines, the trenches excavated for the installation of the fiber cables, and the manholes. The inset diagram illustrates the distribution of the different types of cables within the trenches.

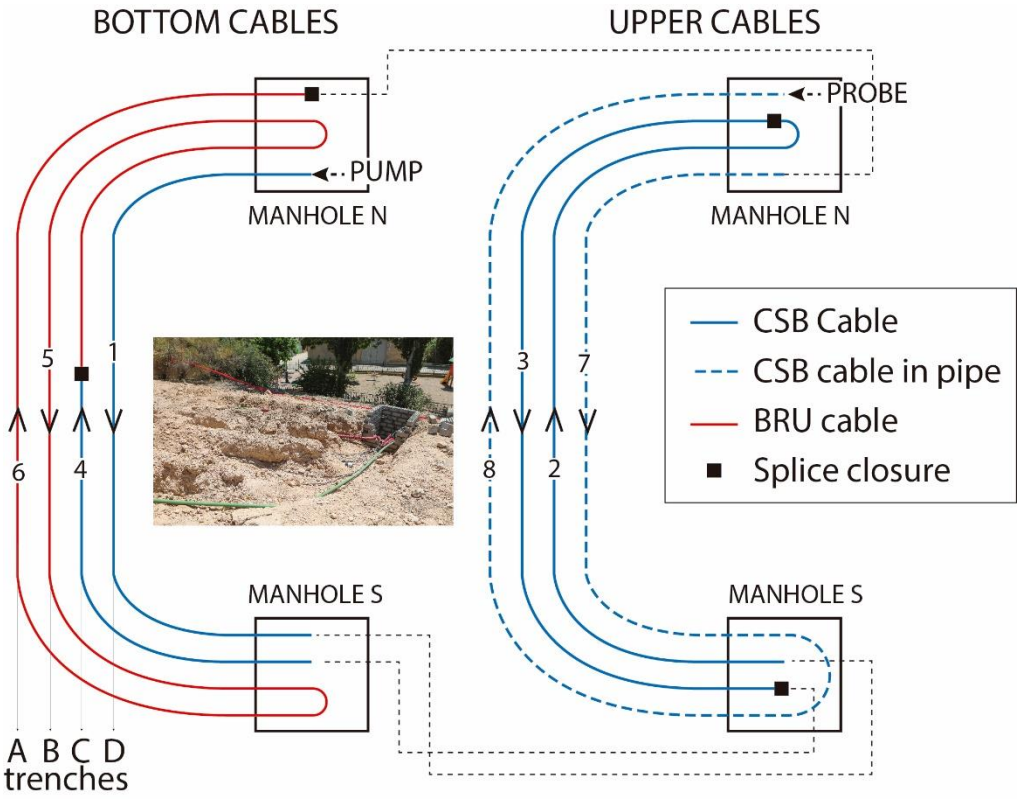

Figure 5. Sketch showing the layout of the fiber cables in the bottom and upper level of the trenches. Numbers and arrows indicate the sequence of cable sections within the loop and the optic path. Inset shows the trenches, cables and manhole S.

The distributed BFS along the fiber cables was measured with a portable interrogator installed in each measurement campaign. The device was designed and encased in a solid box by the company Aragon Photonics Labs, following the scheme described by Domínguez-López et al. (2014). The eight measurement campaigns cover 624 days, extending from 18 June 2020 to 25 March 2022. Data collection was carried out connecting the interrogator to the cables in manhole N. A total of ten measurements were systematically taken in each campaign. Data with higher noise and uncertainty were discarded on the basis of a repeatability analysis. The recorded BFS corresponds to the frequency difference between the pump and the counter-propagating probe when the amplification of the latter is maximum. The temperature contribution to the BFS recorded along the cables buried in the soil was compensated by using the spatially distributed BFS measured in the cables placed within pipes. In this slow-moving sinkhole, these cables can be assumed to remain unaffected by sinkhole-related deformation. Temperature variations between campaigns and along the cable were resolved using the BFS values recorded in each campaign and the temperature coefficient of the cable. Due to the

limited length of the layout and its homogeneity, minor temperature variations across the sinkhole have been observed. Based on the temperature data, the sole contribution of the thermo-optic effect to the BFS can be determined by considering the temperature coefficient of the bare fiber. Finally, by subtracting this amount from the BFS measured in the cables buried in soil, the strain contribution was isolated. The strain provides a measurement of the relative elongation/contraction at each point.

Strain is obtained from the variation of the BFS between campaigns. The strain sensitivity coefficient for standard single mode fibers is widely established at about 0.05 MHz/με (Horiguchi et al., 1989; Ohno et al., 2001). Due to intrinsic dependence of the performance on the fiber layout, the quality of the measurements was assessed in each campaign. Based on the analysis of the BFS recovered for the whole set of measurements taken in each campaign, a maximum uncertainty of 18 με can be established for the measuring system. The sampling spatial resolution was set to 1 m, being determined by the acquisition rate of 100 MS/s. The gauge length is given by the 2 m long segment of the fiber covered by the optical pulse, which is determined by its temporal width, set to 20 ns. In order to reliably compare the data collected on the leveling lines and the fiber cables deployed in the trenches, the position of tie points in the latter was determined by thermal stimulation with ice cube bags. The precise location of the stimulation point was easily determined by comparing data collected before placing the ice and after some time, when the temperature of the cables had dropped substantially at those locations. The distribution of the measured BFS between the tie points was established by linear interpolation.

In the investigated ground deformation phenomenon, characterized by slow sagging subsidence dominated by vertical displacement, we consider that the deformation of the fiber (ΔH) at each point is:

$$\Delta H(x) = \int_0^x \varepsilon(l) \cdot dl$$

where ε is the measured strain and l is x. Additionally, in settings with limited tensile extension, the rigidity of the cable may play a relevant role in the strain profile where the system is under tension (Peled et al., 2013; Zhang et al., 2020). **Figure 6** shows the theoretical distribution of displacement and strain values related to subsidence deformation with a Gaussian shape. The graphs show the coincidence of the maximum values of displacement and strain, corresponding to an inflection point in the deformation curve. Additionally, the strain shows negative values in the central sector of the subsidence zone (contraction) and positive values at the margins

(elongation). This strain profile under a gaussian vertical displacement has been previously modeled for pipelines (Vorster et al., 2005) and also empirically validated (Klar et al., 2014) for man-made induced ground displacements. It was also reproduced in laboratory experiments for small vertical displacements (Liu et al., 2017) Moreover, this deformation pattern is commonly observed in active sagging sinkholes (De Waele and Gutiérrez, 2022). Therefore, the strain measured in the fiber can be considered as a proxy for sinkhole-related subsidence and can be compared with vertical displacement measured in adjacent high-precision leveling lines.

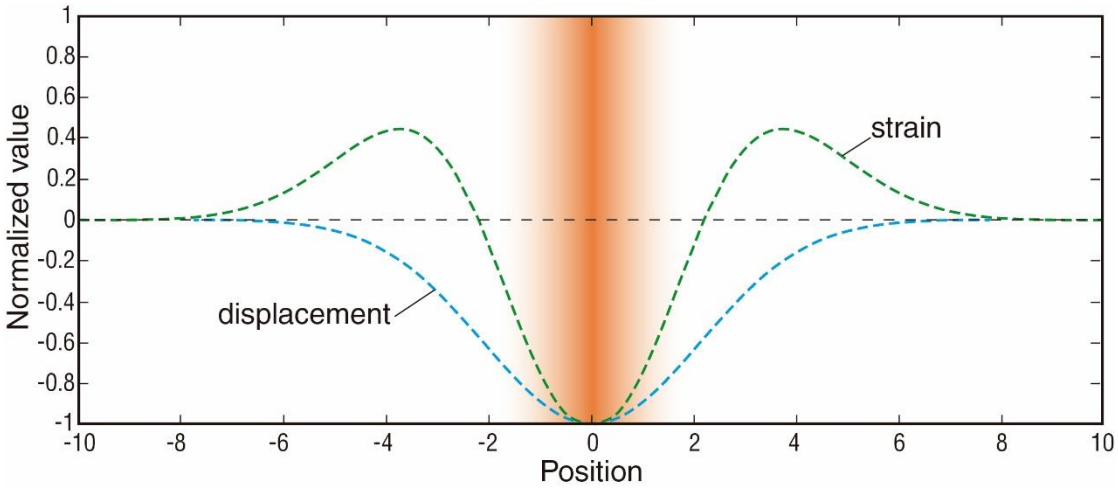

Figure 6. Theoretical distribution of the strain and deformation magnitudes associated with a punctual subsidence with a Gaussian shape.

Two leveling lines 136 m long were installed at the edges of the dike crest, coinciding with the section of the dike monitored with optical fiber. Leveling line W lies next to trench A on the river side, and leveling line E is contiguous to trench D on the village side, with a separation between the leveling lines and the contiguous trenches of 1.5 m (**Fig. 4**). The leveling lines consist of 18 corrugated iron rods 50 cm long with a spacing of 8 m, driven into the ground around 47 cm. The nine leveling campaigns cover a time period of 736 days, spanning from 19 May 2020 to 25 May 2022, with measurements taken around every three months (**Table 1**). This period includes an ordinary flood that peaked on 14 December 2021. Despite the investigated section of the dike being restricted to traffic, some benchmarks were found damaged in the campaigns of 22 September 2021 and 20 December 2021. This damage caused by maintenance work and transit of lorries of the Emergency Army Unit during the December 2021 flood. The benchmarks were replaced to re-establish measurements in the following campaigns.

Vertical ground displacement was measured by high-precision leveling using a digital level (Leica DNA03) mounted on a tripod with fixed-length legs, and a 2 m long bar-coded invar staff (Leica GPCL2). An utmost accuracy with a standard deviation of 0.3 mm per kilometer in double-run

leveling can be achieved with this equipment. The elevation difference between adjacent benchmarks was measured stationing the digital level at a central position and collecting backsight and foresight measurements in both fore and back runs (backward-foreward method based on double leveling). This approach minimizes the errors related to the displacement of the collimation axis and to refraction (ISO 17123_2, 2001). The measured values were considered invalid when the difference between the forward and backward measurements were higher than 0.3 mm. Profiles of cumulative vertical displacement were plotted using the first profile as datum and assuming that the benchmark situated at the initial edge of the line remains stable (e.g., Sevil et al., 2020).

	Leveling line W					Leveling line E			
Dates	Elapsed time (days)	Maximum subsidence (mm)	Average subsidence (mm)	Maximum subsidence rate (mm/yr)	Average subsidence rate (mm/yr)	Maximum subsidence (mm)	Average subsidence (mm)	Maximum subsidence rate (mm/yr)	Average subsidence rate (mm/yr)
19/05/2020	0	DATUM	DATUM	DATUM	DATUM	DATUM	DATUM	DATUM	DATUM
24/09/2020	128	3.680	1.295	10.494	3.692	1.800	0.824	5.133	2.351
09/12/2020	76	1.750	0.612	8.405	2.940	2.155	1.258	10.350	6.041
23/03/2021	104	+0.077	+1.548	+0.272	+5.433	0.895	0.315	3.141	1.106
18/06/2021	87	1.918	0.947	8.045	3.975	0.820	0.401	3.440	1.684
22/09/2021	96	1.455	0.638	5.532	2.425	1.890	1.098	7.186	4.176
20/12/2021	89	8.785	3.513	36.028	14.409	4.750	1.207	19.480	4.950
07/03/2022	77	3.430	1.238	16.259	5.871	10.720	2.810	50.816	13.320
25/05/2022	79	1.755	0.838	8.109	3.873	0.610	0.204	2.818	0.941

Table 1. High-precision leveling data. Measurement dates, elapsed time between consecutive measurements, maximum and average subsidence, and maximum and average subsidence rates for the time interval between successive campaigns.

6. Results

6.1 High-precision leveling

The temporal span of the leveling data covers the whole measurement period of the optical fiber data(**Table 1**). The vertical deformation profiles of leveling line W, situated on the river side, show a section affected by subsidence around 50 m long, between benchmarks 9 and 16, with the point of maximum subsidence persistently situated at benchmark 12 (**Fig. 7**). The profiles of leveling line E indicate active subsidence along more than 110 m, extending from benchmark 3 to an unknown point beyond the edge of the line at benchmark 18. The point of maximum subsidence is located around benchmark 12, coinciding with that of the opposite line.

Both lines show a clear subsidence-acceleration phase associated with the Ebro River flood that peaked in December 2021. The maximum subsidence rate at leveling line W increased from background values of 5-10 mm/yr to 36 mm/yr (benchmark 12) (**Fig. 7, Table 1**). Similarly, the

438 average subsidence rate computed in this line considering the control points situated within the
439 subsidence section increased from around 3 mm/yr to 14 mm/yr. Although a significant number
440 of measurements were lost in leveling line E during December 2021, this line also shows an
441 increase in the maximum and average subsidence rates associated with the flood, from 3-10 to
442 20-50 mm/yr, and from 1-6 to 13 mm/yr, respectively. The subsidence acceleration in leveling
443 line E shows some delay response with respect to the line located on the river side. Subsidence
444 acceleration in the Alcalá sinkhole induced by floods has been previously documented with
445 leveling and terrestrial laser scanner data (Benito-Calvo et al., 2018; Gutiérrez et al., 2019).
446 During the high stage of the flood, the water level in the river is situated above the village, and
447 water can flow through and beneath the dike causing internal erosion (i.e., siphoning). In the
448 recession stage, the drop of the groundwater level involves a decrease in the effective weight
449 of sediments above cavities and karstification zones (i.e., buoyancy loss).

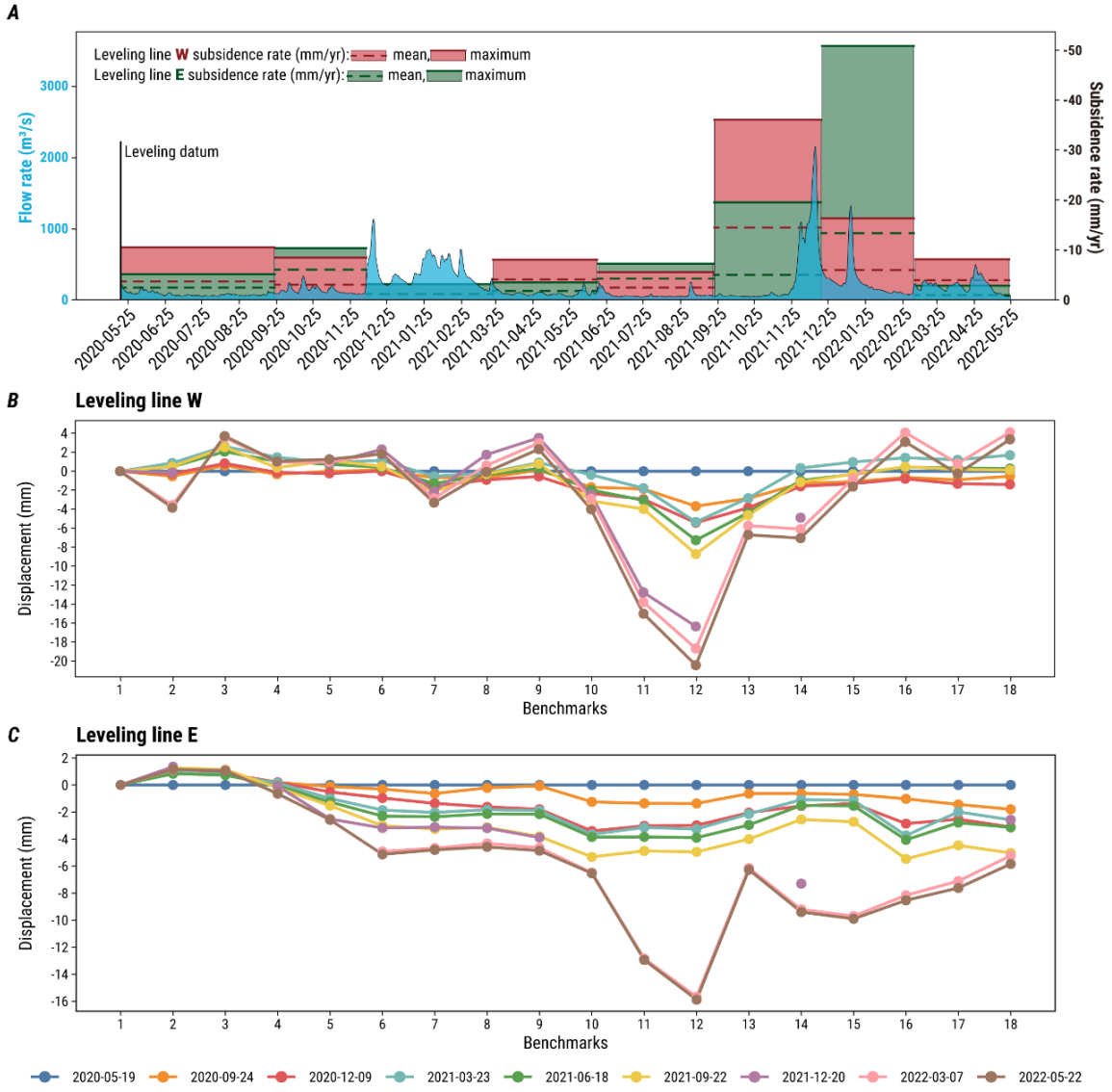

450

Figure 7. High-precision leveling data. A: Temporal variation of maximum and average subsidence rates recorded in leveling lines W and E and flow rate of the Ebro River recorded at Zaragoza city gauging station (30 km downstream of Alcalá). Note subsidence acceleration associated with the flood that peaked in December 2021. B: Profiles of cumulative vertical displacement in leveling line W. C: Profiles of cumulative vertical displacement in leveling line E.

6.2 BOTDA fiber sensing

In order to independently and quantitatively assess the performance of the BOTDA optical fiber, and for the sake of brevity, here we compare vertical displacement data measured in leveling line W with the strain recorded in the two adjacent trenches A, and B. These trenches, situated around 1.5 and 3 m apart from leveling line W, contain two BRU cable sections at the bottom of the trenches, and a CSB cable section in the upper level of trench B (**Figs. 4, 5**). We have selected data collected along the western river side of the dike because leveling line W: (1) provides the most complete displacement data, barely affected by the temporal loss of benchmarks; (2) includes the whole section affected by subsidence, with relatively well defined limits; and (3) clearly captures the subsidence acceleration associated with the December 2021 flood (**Fig. 7B**). It should be noted that the position of the edges of the subsidence area in leveling lines W and E are markedly different, indicating a rapid eastward enlargement (**Fig. 7**).

The strain recorded by the BRU cable in the bottom of trench A shows an overall spatial correlation with the subsidence measured in leveling line W (**Fig. 8**): (1) negative strain values dominate in the area affected by active subsidence showing a well-defined trough; (2) the highest negative strain values coincide with the location of maximum subsidence rate; and (3) the margins of the subsidence area are dominated by positive strain, expressed as ridges in the graphs. This general pattern indicative of contraction in the inner part of the subsidence bowl (trough) and extension at the margins (ridges) is consistent with the strain profile expected for slow subsidence (Liu et al., 2017) (**Fig. 6**), and with evidence of deformation observed in sagging sinkholes (De Waele and Gutiérrez et al., 2022). The strain recorded in the BRU cable of trench A over the different campaigns also shows some temporal correlation with the subsidence data measured by leveling. The negative strain in the area of maximum subsidence shows a substantial increment associated with the December 2021 flood (measurement of 30 December 2021), followed by an interval with very limited variation after the flood, showing a similar temporal pattern to the displacement measured by leveling. The increment between September

and December 2021 at the highest strain point was 37% higher than the average of the differences between previous consecutive campaigns.

The strain recorded in the BRU and CSB cables deployed in trench B also show a reasonably good spatial and temporal correlation with the leveling displacement data, including negative and positive values in the inner and marginal sectors of the subsidence area, respectively, a maximum negative value approximately coinciding with the point of maximum subsidence rate, and significant strain increase associated with the flood (**Fig. 8**). The offset between the highest strain recorded in the BRU and CSB cables of trench B and the point with highest subsidence rate can be attributed to several non-exclusive factors: (1) low resolution of the leveling data, with a spacing between benchmarks of 8 m; (2) cable location errors introduced through the linear interpolation of the strain data between the tie points identified by thermal stimulation; (3) variations in the position of the most rapid subsidence point across the dike. In the case of the BRU and CSB cables of trench B, the flood-related increment between September and December 2021 at the highest strain point was 111% and 83% higher than the average of the differences between previous consecutive campaigns, respectively.

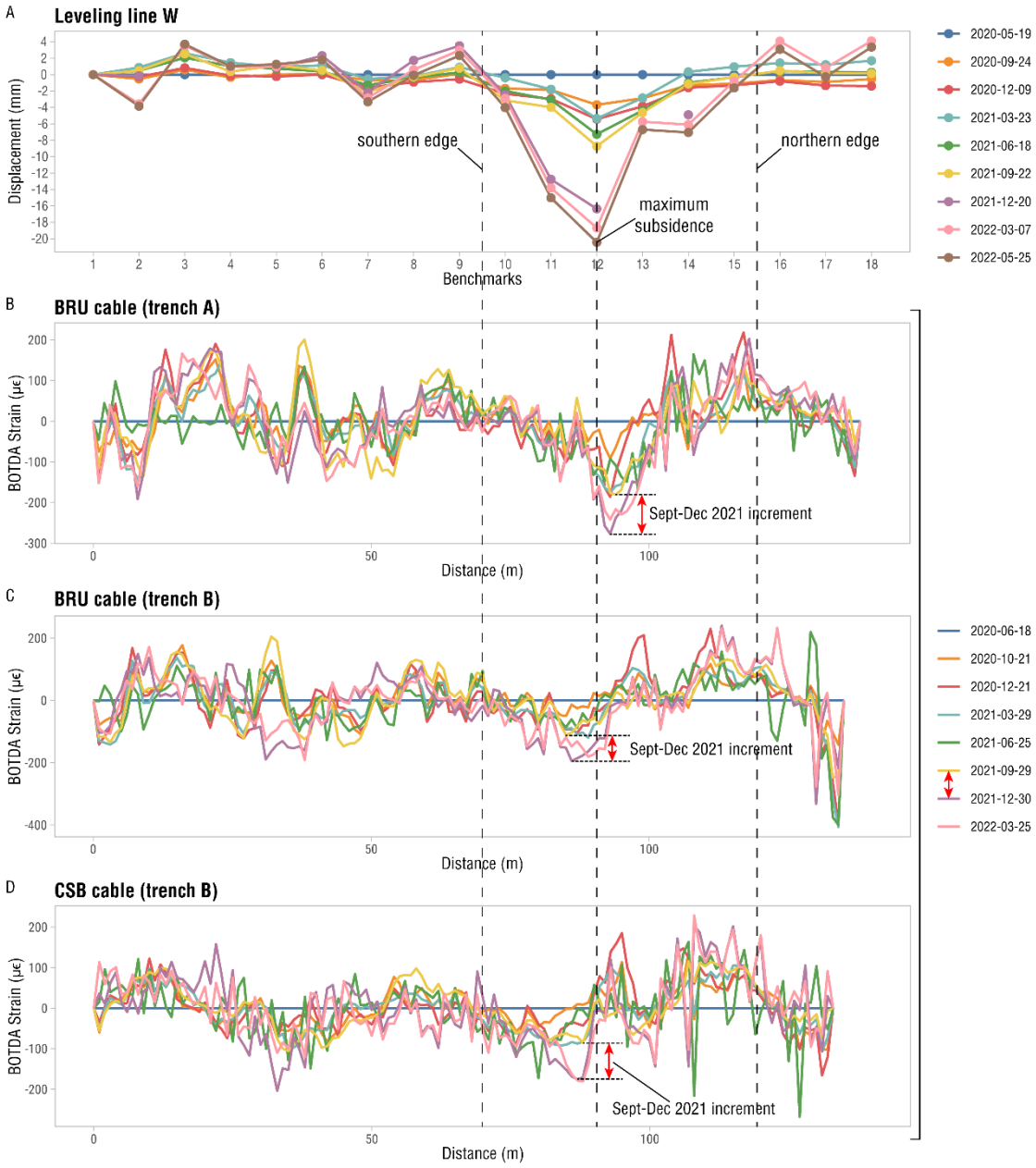

Figure 8. Cumulative subsidence measured in leveling line W and strain recorded in the BRU cable of trench A and the BRU and CSB cables of trench B. Note the overall spatial and temporal correlation, with a substantial strain increment correlative to the accelerated subsidence phase associated with the December 2021 flood. The same colors are used for measuring campaigns with close dates.

7. Discussion and conclusions

The type of sinkhole (i.e., subsidence mechanism, kinematics) may have a strong influence on the capability of DOFS to detect subsidence activity and its performance (**Figs. 1 and 2**). The

most challenging situation is probably that of sagging sinkholes characterized by slow progressive displacement within vaguely-edged subsidence areas and limited lateral deformation gradients. More clear strain signatures can be expected in collapse and suffosion sinkholes that typically display sharp lateral deformation gradients related to localized deformation (i.e., steeply dipping failure planes and shear zones, folds with narrow hinge zones). Greater spatial resolution is needed for the latter sinkholes due to their smaller size. Moreover, the installation of relatively deep fiber cables could allow the detection of precursory deformation of collapse sinkholes related to the stoping of cavities that have considerably advanced, thus increasing the success rate of early warning systems. To our knowledge, previous studies on the application of DOFS to sinkhole monitoring present data from experiments that address subsidence associated with artificial or virtual cover collapse sinkholes: (1) collapse sinkholes that are less than 1.5 m across reproduced with containers; (2) sinkhole-related deformation simulated by applying vertical loads; and (3) numerical models that predict both ground deformation above cavities and the signal recorded by optical fiber sensors. Although the results of these artificial experiments might be applicable to real sinkholes, it is highly desirable to test this monitoring technique in active sinkholes of different types under natural conditions. The previous experiments always consider the most favorable subsidence scenario, namely collapse sinkholes of known position characterized by rapid subsidence and sharp lateral deformation gradients (**Figs. 1 and 2**).

High-precision leveling data indicate that the Alcalá sinkhole is characterized by sagging subsidence along sections tens of meters across, with poorly-defined edges, faint lateral deformation gradients, and very low subsidence rates. Leveling line W indicates maximum and average subsidence rates of 5-36 mm/yr and 3-14 mm/yr, respectively. Despite the challenging subsidence scenario, the strain recorded by both the BRU and CSB fiber optic cables captures the subsidence process with a reasonably good spatial and temporal correlation. The section affected by slow sagging subsidence is expressed in the strain profiles by: (1) troughs of negative values (contraction) in the area affected by subsidence, with the maximum strain associated with the maximum deformation point; and (2) lateral ridges of positive values (extension) in the marginal zones. This pattern of inner contraction and marginal extension is consistent with the deformation features commonly associated with sagging sinkholes. Passive bending (i.e., sagging) involves radial contraction, which is counterbalanced at the margins by extension. Moreover, moment bending related to the flexing process tends to produce contraction and extension in the inner arch of synforms (sinkhole center) and the outer arch of antiforms (sinkhole margin), respectively (Gutiérrez et al., 2012, 2018; De Waele and Gutiérrez, 2022). The

temporal series also capture the subsidence acceleration phase associated with a flood. Maximum subsidence rates increased from 5-10 mm/yr to 36 mm/yr and strain values at the points of greatest negative strain increased around 40-110%. Notwithstanding the relatively good spatial and temporal match between the strain data and the precisely measured subsidence, it should be admitted that, in this difficult case and at this stage, the unambiguous identification of the active subsidence zone with the optical fiber data alone would be challenging. Probably, a more obvious subsidence-related strain signature could be obtained improving the coupling between the cables and the ground, made up of loose sand and gravel. Recent studies, (Möller et al., 2022, Della Ragione et al., 2023) have demonstrated that although the coupling mechanism affects the quantitative value of the strain measured by the fiber, its spatial profile mimics the soil deformation. Much better results can be expected in other sinkhole types with greater lateral deformation gradients.

The reviewed literature and the results obtained in this work in a real sinkhole with adverse subsidence features suggest that distributed optical fiber sensors might be a useful technique for monitoring subsidence related to sinkhole activity and even detecting precursory deformation preceding the occurrence of catastrophic collapse, functioning as an early-warning system. This long-range and distributed optical monitoring technique can be especially suitable for surveying linear infrastructure such as roads, railways, pipelines, or dykes. Some of the advantages of the BOTDA optical fiber sensors for subsidence monitoring include: (1) It permits long-range (tens of kilometers), distributed monitoring to resolve the spatial and temporal patterns of the subsidence process, including accelerations in the subsidence rates (Xu et al., 2017; this work). In contrast with Time Domain Reflectometer (TDR), which is a breakpoint monitoring technology (Chen et al., 2020), it permits the detection of subsidence related to multiple sinkholes. (2) Measurements can be obtained automatically, remotely and in real-time, offering the option of implementing early-warning systems (Shefchik et al., 2011). (3) High measurement accuracy (10 με) and sampling resolution (e.g., Chen et al., 2020). (4) High durability and resistance to corrosion and heat; the optical fiber can be protected in packed cables to prevent damage. (5) Electromagnetic interference immunity. Perhaps the main limitation is that the measured Brillouin frequency shift can be related not only to sinkhole-related deformation, but also to other natural and anthropogenic factors that need to be filtered out, such as temperature, loading induced by traffic, or heterogeneous deformations related to temperature and moisture conditions in the soil (Linker and Klar, 2017). In some circumstances it may be difficult to differentiate signals related to incipient sinkholes from those produced by other disturbances. Further exploratory works in real sinkholes with different subsidence

577 mechanisms and kinematic features are needed to better assess the practical capabilities of the
578 technique.

579

580 **Acknowledgements**

581 This work has been supported by projects CGL2017-85045-P, PID2021-123189NB-I00, and DI-
582 17-09169 (Ministerio de Ciencia e Innovación, Gobierno de España). Government of Aragón
583 (Reference Group T20_20R). J.S. has a predoctoral contract (PRE2018-084240) co-financed by
584 the Spanish Government and the European Social Fund (ESF). The authors are very grateful to
585 the City Hall of Alcalá de Ebro and the Confederación Hidrográfica del Ebro for granting
586 permission to install the monitoring system. We are very grateful to an anonymous reviewer
587 and Dr. Anthony Copper for their helpful comments.

588

589 **References**

590 Assaf, K., Idan, D., Raphael, L., 2014. Monitoring tunneling induced ground displacements using
591 distributed fiber-optic sensing. Tunn. Undergr. Space Technol. 40, 141-150.
592 Al-Halbouni, D., Holohan, E.P., Saberi, L., Alrshdan, H., Sawarieh, A., Closson, D., Walter, T.R.,
593 Dahm, T., 2017. Sinkholes, subsidence and subrosion on the eastern shore of the Dead Sea
594 as revealed by close-range photogrammetry survey. Geomorphology 285, 305–324.
595 Baer, G., Magen, Y., Nof, R.N., Raz, E., Lyakhovsky, V., Shalev, E., 2018. InSAR measurements and
596 viscoelastic modelling of sinkhole precursory subsidence: Implication for sinkhole formation,
597 early warning and sediment properties. Journal of Geophysical Research: Earth Surface 123,
598 678-693.
599 Benito-Calvo, A., Gutiérrez, F., Martínez-Fernández, A., Carbonel, D., Karampaglidis, T., Desir, G.,
600 Sevil, J., Guerrero, J., Fabregat, I., García-Arnay, Á, 2018. 4D monitoring of active sinkholes
601 with Terrestrial Laser Scanner (TLS). A case study in the evaporite karst of the Ebro Valley, NE
602 Spain. Remote Sensing 10, 571.
603 Chen, H., He, J., Xue, Y., Zhang, S., 2020. Experimental study on sinkhole collapse monitoring
604 based on distributed rillouin optical fiber sensor. Optik 216, 164825.
605 Culverhouse, D., Farahi, F., Pannell, C.N., Jackson, D.A., 1989. Potential of stimulated Brillouin
606 scattering as sensing mechanism for distributed temperature sensors. Electronics Letters 14,
607 913-915.
608 De Waele, J., Gutiérrez, F., 2022. Karst Hydrogeology, Geomorphology and Caves. Wiley.

609 Della Ragione, G., Bilotta, E., Xu, X., da Silva Burke, T.S., Möller, T., Abadie, C.N., 2023. Numerical
610 investigation of fibre-optic sensing for sinkhole detection. Géotechnique 1–14.
611 Desir, G., Gutiérrez, F., Merino, J., Carbonel, D., Benito-Calvo, A., Guerrero, J., Fabregat, I., 2018.
612 Rapid subsidence in damaging sinkholes: Measurements by high-precision leveling and the
613 role of salt dissolution. Geomorphology 303, 393-409.
614 Domínguez-López, A., López-Gil, A., Martín-López, S., González-Herráez, M., 2014. Signal-to-
615 Noise Ratio Improvement in BOTDA Using Balanced Detection. IEEE Photonics
616 Technology Letters 26, 338–341.
617 Guan, Z.D., Jiang, X.Z., Wu, Y.B., Pang, Z.Y., 2015. Study on monitoring and early warning of karst
618 collapse based on BOTDR technique. In: Doctor, D.H., Land, L., Stephenson, J.B. (Eds.),
619 Proceedings of the 14th Multidisciplinary Conference on Sinkholes and the Engineering and
620 Environmental Impacts of Karst. National Cave and Karst Research Institute, pp. 407–414.
621 Gutiérrez, F. (2016). Sinkhole hazards. In: Oxford Research Encyclopedia of Natural Hazard
622 Science. Oxford: Oxford University Press. Available at:
623 https://oxfordre.com/naturalhazardscience/view/10.1093/acrefore/9780199389407.001.0
624 001/acrefore-9780199389407-e-40.
625 Gutierrez, F., Carbonel, D., Guerrero, J., McCalpin, J.P., Linares, R., Roque, C., Zarroca,C., 2012.
626 Late Holocene episodic displacement on fault scarps related to interstratal dissolution of
627 evaporites (Teruel Neogene Graben, NE Spain). J. Struct. Geol. 34, 2–19.
628 Gutiérrez, F., Mozafari, M., Carbonel, D., Gómez, R., Raeisi, E., 2015. Leakage problems in dams
629 built on evaporites. The case of La Loteta Dam (NE Spain), a reservoir in a large karstic
630 depression generated by interstratal salt dissolution. Engineering Geology 185, 139-154.
631 Gutierrez, F., Zarroca, M., Linares, R., Roque, C., Carbonel, D., Guerrero, J., McCalpin, J.P., Comas,
632 X., Cooper, A.H., 2018. Identifying the boundaries of sinkhole and subsidence areas and
633 establishing setback distances. Eng. Geol. 233, 255–268.
634 Gutiérrez, F., Benito-Calvo, A., Carbonel, D., Desir, G., Sevil, J., Guerrero, J., Martínez-Fernández,
635 A., Karampaglidis, T., García-Arnay, A., Fabregat, I., 2019. Review on sinkhole monitoring and
636 performance of remediation measures by high-precision leveling and terrestrial laser scanner
637 in the salt karst of the Ebro Valley, Spain. Engineering Geology 248, 283-308.
638 Gutiérrez, F.; Sevil, J.; Migon, P., 2022. Landslides in the Remolinos gypsum escarpment (NE
639 Spain). Controls imposed by stratigraphy, fluvial erosion and interstratal salt dissolution.
640 Landslides, submitted.
641 Hartog, A.H., 2017. An Introduction to Distributed Optical Fiber Sensors. CRC Press, Boca Raton.

642 Horiguchi, T., Kurashima, T., Tateda, M., 1989. Tensile strain dependence of Brillouin frequency
643 shift in silica optical fibers. IEEE Photonics Technology Letters 1, 107-108.
644 Inaudi, D., 2014. Sensing solutions for assessing the stability of levees, sinkholes and landslides.
645 In: Wang, M.L., Lynch, J.P., Sohn, H. (Eds.), Sensor Technologies for Civil Infrastructures, pp.
646 396-421.
647 ISO 17123-2, 2001. Optics and optical instruments. In: Field Procedures for Testing Geodetic and
648 Surveying Instruments. Part 2: Levels. Switzerland, Geneva, pp. 14.
649 Jiang, X., Gao, Y., Wu, Y., Lei, M., 2016. Use of Brillouin optical time domain reflectometry to
650 monitor soil-cave and sinkhole formation. Environmental Earth Science 75, 1-8.
651 Jones, C.E., Blom, R.G., 2014. Bayou Corne, Louisiana, sinkhole: Precursory deformation
652 measured by radar interferometry. Geology 42, 111–114.
653 Klar, A., Dromy, I., Linker, R., 2014. Monitoring tunneling induced ground displacements using
654 distributed fiber-optic sensing. Tunnelling and Underground Space Technology 40, 141-150.
655 Lanticq, V., Bourgeois, E., Magnien, P., Dieleman, L., Vinceslas, G., Sang, A., Delepine-Lesoille, S.,
656 2009. Soil-embedded optical fiber sensing cable interrogated by Brillouin optical time-
657 domain reflectometry (B-OTDR) and optical frequency-domain reflectometry (OFDR) for
658 embedded cavity detection and sinkhole warning system. Measurement Science and
659 Technology 20, 034018.
660 Linker, R., Klar, A., 2017. Detection of sinkhole formation by strain profile measurements using
661 BOTDR: Simulation study. Journal of Engineering Mechanics 143, B4015002.
662 Liu, J., Wang, Y., Lu, Y., Wei, J., Kanungo, D.P., 2017. Application of Distributed Optical Fiber
663 Sensing Technique in Monitoring the Ground Deformation. Journal of Sensors 2017,
664 e6310197.
665 Malovichko, D.A., Dyagilev, R.A., Shulakov, D.Y., Butyrin, P.G., Glebov, S.V., 2009. Seismic
666 monitoring of large-scale karst processes in a potash mine. In: Tang, C.A. (Ed.), Controlling
667 Seismic Hazard and Sustainable Development in Deep Mines. Rinton Press, pp. 989–1002.
668 Möller, T., da Silva Burke, T.S., Xu, X., Della Ragione, G., Bilotta, E., Abadie, C.N., 2022. Distributed
669 fibre optic sensing for sinkhole early warning: experimental study. Géotechnique 1–15.
670 Naruse, H., Uehara, H., Deguchi, T., Fujihashi, K., Onishi, M., Espinoza, R., Guzmán, C., Pardo, C.,
671 Ortega, C., Pinto, M., 2007. Application of a distributed fibre optic strain sensing system to
672 monitoring changes in the state of an underground mine. Measurement Science and
673 Technology 18, 3202-3210.
674 Ohno, H., Naruse, H., Kihara, M., Shimada, A., 2001. Industrial Applications of the BOTDR Optical
675 Fiber Strain Sensor. Optical Fiber Technology 7, 1, 45-64.

676 Peled, Y., Motil, A., Kressel, I., Tur, M., 2013. Monitoring the propagation of mechanical waves
677 using an optical fiber distributed and dynamic strain sensor based on BOTDA. Optics Express
678 21, 10697-10705.
679 Quiles, E., 2007. Estudio del subsuelo. Alcalá de Ebro (Zaragoza). Ministerio de Medio Ambiente.
680 Confederación Hidrográfica del Ebro. Unpublished report.
681 Salvany, J.M., 2009. Geología del yacimiento glauberítico de Montes de Torrero. Universidad de
682 Zaragoza, Zaragoza.
683 Salvany J.M., García-Veigas, J., Ortí, F., 2007. Glauberite-halite association of the Zaragoza
684 Gypsum Formation (Lower Miocene, Ebro Basin, NE Spain). Sedimentology 54, 443–467.
685 Shefchik, B., Tomes, R., Belli, R., 2011. Salt Cavern Monitoring System for Early Warning of
686 Sinkhole Formation. Geotechnical News 29, 30-33.
687 Schwendel, A.C., Cooper, A.H., 2021. Meander chute cutoff at an alluvial river facilitated by
688 gypsum sinkholes. Geomorphology 393, 107944.
689 Sevil, J., Gutiérrez, F., Carnicer, C., Carbonel, D., Desir, G., García-Arnay, A., Guerrero, J., 2020.
690 Characterizing and monitoring a high-risk sinkhole in an urban area underlain by salt through
691 non-invasive methods: Detailed mapping, high-precision leveling and GPR. Engineering
692 Geology 272, 105641.
693 Sevil, J., Benito-Calvo, A., Gutiérrez, F., 2021. Sinkhole subsidence monitoring combining
694 terrestrial laser scanner and high-precision leveling. Earth Surface Processes and Landforms
695 46, 1431-1444.
696 Theron, A., Engelbrecht, J., Kemp, J., Kleynhans, W., Turnbull, T., 2017. Detection of sinkhole
697 precursors through SAR interferometry: radar and geological considerations. IEEE Geosci.
698 Remote Sens. Lett. 14, 871–875.
699 Vorster, E., Klar, A., Soga, K., Mair, R., 2005. Estimating the Effects of Tunneling on Existing
700 Pipelines. Journal of Geotechnical and Geoenvironmental Engineering. 131, 1399-1410.
701 Xin, Y., Li, X., Zhang, W., Wang, Q., 2021. Characterizing the deep pumping-induced subsidence
702 against metro tunnel using vertically distributed fiber-optic sensing. Environmental Earth
703 Sciences 80, 1-15.
704 Xu, J., He, J., Zhang, L., 2017. Collapse prediction of karst sinkhole via distributed Brillouin optical
705 fiber sensor. Measurement 100, 68-71.
706 Yeniay, A., Delavaux, J.-M., Toulouse, J., 2002. Spontaneous and stimulated Brillouin scattering
707 gain spectra in optical fibers. Journal of Lightwave Technology 20, 1425–1432.
708 Zhang, Z., Guan, P., Xu, J., Wang, B., Li, H., Dong, Y., 2020. Horizontal Loading Performance of
709 Offshore Wind Turbine Pile Foundation Based on DPP-BOTDA. Applied Sciences 10, 492.

710 Zhao, M., Yi, X., Zhang, J., Lin, C., 2021. PPP-BOTDA distributed optical fiber sensing technology
711 and its application to the Baishuihe landslide. Frontiers in Earth Science 9, 660918.
712 Zhende, G., Xiaozhen, J., Ming, G., 2013. A calibration test of karst collapse monitoring device by
713 optical time domain reflectometry (BOTDR) technique. In: Land, L., Doctor, D.H., Stephenson,
714 J.B. (Eds.), Proceedings of the 13th Multidisciplinary Conference on Sinkholes and the
715 Engineering and Environmental Impacts of Karst. National Cave and Karst Research Institute.
716 Carlsbad, New Mexico, pp. 71–77.
717 Zhou, Z., He, J., Yan, K., Ou, J., 2008. Fiber-reinforced polymer-packaged optical fiber sensors
718 based on Brillouin optical time-domain analysis. Optical Engineering 47, 014401.